

**Supporting Information of
“Ultra-confined plasmonic hotspots inside graphene nanobubbles”**

Z. Fei^{1,2,3*}, J. J. Foley IV^{2,4}, W. Gannett^{5,6}, M. K. Liu^{1,7}, S. Dai¹, G. X. Ni¹, A. Zettl^{5,6}, M. M. Fogler¹, G. P. Wiederrecht², S. K. Gray², D. N. Basov^{1,8}

¹Department of Physics, University of California, San Diego, La Jolla, 92093, USA

²Center for Nanoscale Materials, Argonne National Laboratory, Argonne, Illinois 60439, USA

³Department of Physics and Astronomy, Iowa State University, Ames, Iowa 50011, USA

⁴Department of Chemistry, William Paterson University, Wayne, New Jersey, 07470, USA

⁵Department of Physics, University of California at Berkeley, Berkeley, California 94720, USA

⁶Materials Sciences Division, Lawrence Berkeley National Laboratory, Berkeley, California 94720, USA

⁷Department of Physics and Astronomy, Stony Brook University, Stony Brook, New York, 11794.

⁸Department of Physics, Columbia University, New York, NY 10027, USA.

*E-mail: (Z.F.) zfei@iastate.edu

List of contents

1. Nano-infrared imaging experiments
2. Sample preparation and characterization
3. Graphene nanobubbles
4. Calculation of the local plasmon wavelength
5. FDTD simulation
6. Real-space simulation of hotspot patterns in nanobubbles

1. Nano-infrared imaging experiments

The nano-infrared (IR) imaging experiments introduced in the main text were performed at UCSD by using a scattering-type scanning near-field optical microscope (s-SNOM). Our s-SNOM is a commercial system (neaspec.com) equipped with continuous wave mid-IR quantum cascade lasers (daylightsolutions.com). The unit for the IR frequency used in the work is wavenumber (cm^{-1}). The typical laser frequency used in the work is $\omega = 910 \text{ cm}^{-1}$, corresponding to a photon energy of 113 meV. The s-SNOM is based on an atomic force microscope (AFM) operating in the tapping mode with a tapping frequency of $\sim 270 \text{ kHz}$ and tapping amplitude of $\sim 50 \text{ nm}$. A pseudo-heterodyne interferometric detection module is implemented in our s-SNOM to extract both the scattering amplitude s and phase ψ of the near-field signal. In the current work, we discuss mainly the amplitude part of the signal that is sufficient to describe the plasmon hotspots. In order to subtract the background signal, we demodulated the near-field signal at the n^{th} harmonics of the tapping frequency ($n = 3$ in the current work). In all the displayed near-field images, we plotted the near-field amplitude normalized to that taken off the nanobubbles on the flat graphene/hBN region. Our nano-IR imaging experiments were performed at ambient conditions.

2. Sample preparation and characterization

Our graphene films were fabricated using a two-step low pressure chemical vapor deposition (CVD) process.¹ We then transferred graphene films to exfoliated hexagonal boron nitride (hBN) crystals on standard SiO_2/Si substrates using a sacrificial polymethyl methacrylate (PMMA) layer.^{2,3} After transferring, we cleaned the PMMA residuals by acetone following by a thermal annealing at $340 \text{ }^\circ\text{C}$ with H_2/Ar . The thermal annealing could potentially induce a tiny compressive strain of about 0.06% on the flat graphene on hBN region away from the nanobubbles.⁴ Such a small strain has negligible effects on both the electronic and plasmonic properties of graphene.^{5,6} Optical microscopy and Raman spectroscopy were used to determine the graphene thickness and to locate graphene/hBN (GBN) and graphene/ SiO_2 (GOS) regions (Figure S1). All our data images about graphene nanobubbles were taken in the graphene/hBN regions.

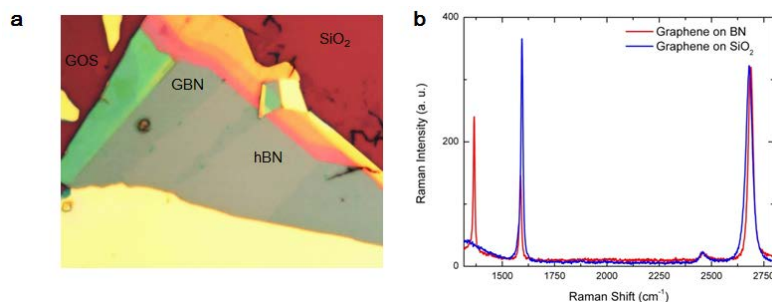


Figure S1. (a) Typical optical image of CVD graphene transferred to exfoliated hBN microcrystals on SiO_2/Si wafers. Here the graphene on hBN and graphene on SiO_2 regions are marked with ‘GBN’ and ‘GOS’ respectively. (b) Raman spectra of graphene on hBN and graphene on SiO_2 .

3. Graphene nanobubbles

The nanobubbles are formed in the graphene on hBN regions after the transferring and annealing processes. The formation of these nanobubbles is believed to be related to the negative thermal expansion coefficient of graphene⁴ as well as residual materials at the graphene/hBN interface.⁷⁻⁹ These residual materials will aggregate together as the filling materials inside the

bubbles. They are originated from interfacing materials of graphene during the transfer process, for example air, water, acetone and PMMA. The follow-up thermal annealing could cause thermal degradation of PMMA into monomer MMA that is normally in the liquid form at ambient temperature.^{10,11} Indeed, previous works about similar nanobubbles have seen evidence of hydrocarbons inside the bubbles.⁹ It was also observed that these residual materials are mobile⁷⁻⁹ and easy to escape or evaporate when nanobubbles were broken.⁹ Moreover, our real-space simulations in Figure S6 suggest that a homogeneous distribution of the filling materials is necessary to reproduce the hotspots patterns observed in our experiments. In our analysis, we consider all possible forms of residual materials. For air or hydrocarbon gas, the permittivity is $\epsilon_m \approx 1.0$. For water,¹² acetone,¹³ and solid PMMA,¹⁴ ϵ_m at $\omega \sim 910 \text{ cm}^{-1}$ is about 1.3, 1.8 and 2.4 at $\omega \sim 910 \text{ cm}^{-1}$, respectively. For other hydrocarbon liquids, though optical constants vary depending on the exact chemical composition, ϵ_m at $\omega \sim 910 \text{ cm}^{-1}$ is commonly far below 4.0 that is the effective permittivity of hBN (Figure S3).¹⁵ The relative smaller permittivity of the bubble medium compared to that of hBN is the major cause of the plasmonic impedance mismatch between graphene nanobubbles and the flat graphene regions.

4. Graphene doping

As shown in Eq. 1 in the main text, carrier density (n) is one essential parameter that determines the plasmon wavevector and hence the plasmon wavelength of graphene. Nevertheless, we believe the doping inhomogeneity (δn) of our graphene samples is a minor effect compared to variations of dielectric environment as discussed in detail in the main text. Compared to detached graphene in the bubble region, the flat support graphene is coupled closely with the substrate, which could possibly cause additional doping to graphene. This is certainly an issue if using SiO₂ as the substrate that could introduce strong doping to graphene.¹⁶ Nevertheless, our graphene sample is sitting on hBN that is a much better substrate with negligible doping effect on graphene, as confirmed by the transport study¹⁷ and very recently a Raman study.¹⁸ In the latter Raman work, the authors investigated graphene on various substrates including hBN as well as suspended graphene over trenches, and their data suggest that the doping level of graphene on hBN is roughly the same as suspended graphene. Therefore, we believe that the carrier density of supported graphene on hBN will not be consistently and largely different from the detached graphene bubble region. Moreover, we wish to emphasize that our graphene samples are highly doped at ambient conditions with a carrier density of $n \approx 3 \times 10^{12} \text{ cm}^{-2}$ according to our simulations, so small doping inhomogeneities (δn) will not affect much the plasmon wavelength (λ_p) of graphene since $\lambda_p \sim (n + \delta n)^{1/2} \approx n^{1/2} (1 + 0.5 \delta n/n)$. For example, a doping inhomogeneity as big as $\delta n = 0.5 \times 10^{12} \text{ cm}^{-2}$ only causes a change of 8% to the plasmon wavelength. This is certainly a small effect compared to the effect due to variation of dielectric environment ($\sim 70\%$) discussed in the main text.

5. Calculation of the local plasmon wavelength

In order to determine the local plasmon wavelength, we first calculate the plasmon dispersion by evaluating numerically the imaginary part of the reflection coefficient $\text{Im}(r_p)$ for the entire graphene/gap/hBN/SiO₂ heterostructure system by using the transfer matrix method (Figure 4 in the main text).¹⁶ Here the gap layer is added to simulate the dielectric medium inside the graphene nanobubble. Based on the calculated dispersion diagrams, we can determine directly the local plasmon wavevector q_p hence the local plasmon wavelength $\lambda_p = 2\pi/q_p$ of graphene. With this method, we produced the gap size (t_{gap}) dependent plasmon wavelengths for graphene as shown in Figure 4a in the main text. We set the hBN thickness to be 150 nm according to our AFM

measurement, but the calculation results do not show noticeable changes for graphene plasmons when the thickness of hBN is above 100 nm.

6. FDTD simulation

We performed rigorous electrodynamics simulations to further investigate the impact of bubble topography and dielectric environment on the plasmon propagation and subsequent hot-spot formation. A commercial-grade simulator based on the finite-difference time-domain (FDTD) method was used to perform the calculations.¹⁷ We considered four different models in our simulations to test the effects of pure dielectric environment (with Model 1 & 2) and pure topography (with Model 3 & 4) on graphene plasmons:

(1) Graphene on an hBN substrate with a cylindrical vacancy to simulate the pure dielectric environment of graphene nanobubbles without introducing topographic features. Detailed sketches about the cylindrical vacancy are plotted in Figure S2. The depth and the diameter of the cylindrical vacancy are set to be 10 nm and 250 nm to match the aspect ratio of the nanobubble ‘A’ in Figure 1 of the main text. Note that the average height of the nanobubble ‘A’ is roughly 10 nm.

(2) Graphene on a flat and intact hBN substrate.

(3) Suspended graphene with a Gaussian-shaped bubble at the center to simulate the pure topographic effects of our graphene bubbles without introducing variations of dielectric environment. The height and the full width at half maximum of the Gaussian-shaped graphene bubble are set to be 20 nm and 125 nm to match the aspect ratio of the nanobubble ‘A’ in Figure 1 of the main text.

(4) Suspended and flat graphene.

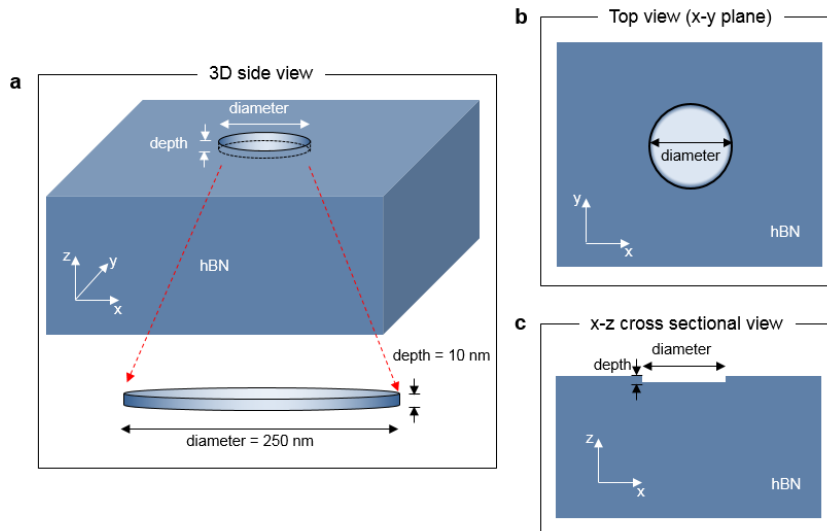


Figure S2. Detailed sketches about Model 1 for FDTD simulation. These sketches include the 3D side view (a), x - y plane top view (b), and x - z plane cross-sectional view (c) about the model. Note that graphene (not shown in these sketches) will be placed right above the hBN surface and vacancy.

In our modeling, the Fermi energy of graphene (E_F) is set to be ~ 0.2 eV corresponding to a 2D optical conductivity $\sigma_{2D} \approx (0.2 + 2i)G_0$ at $\omega = 910 \text{ cm}^{-1}$, where $G_0 = \pi e^2/4h \approx 6.07 \times 10^{-5} \Omega^{-1}$ is the universal optical conductivity of graphene. The effective thickness of graphene is set to be 5 nm, which is two orders of magnitude smaller than the plasmon wavelength. We employ a multi-

resolution grid with a grid spacing of 1 nm in the graphene layer that gradually increases to 10 nm away from graphene. Excitation of graphene plasmons is achieved using a point dipole emitter source with IR frequency around 910 cm^{-1} . The dipole emitter is placed 2 nm above the graphene plane and is polarized along the z -axis (normal to the graphene film). For hBN, we modeled it as an isotropic medium with an effective dielectric constant of $\epsilon_{\text{eff}} \approx 4.0$ at $\omega = 910\text{ cm}^{-1}$. This is validated by the calculated dispersion diagrams in Figure S3 with both effective and realistic dielectric constants ($\epsilon_{\text{ab}} \approx 8.1+0.01i$ and $\epsilon_c \approx 1.7+0.02i$).¹⁸ Here we found that the plasmon wavevector q_p at $\omega = 910\text{ cm}^{-1}$ is roughly the same for both dispersion diagrams.

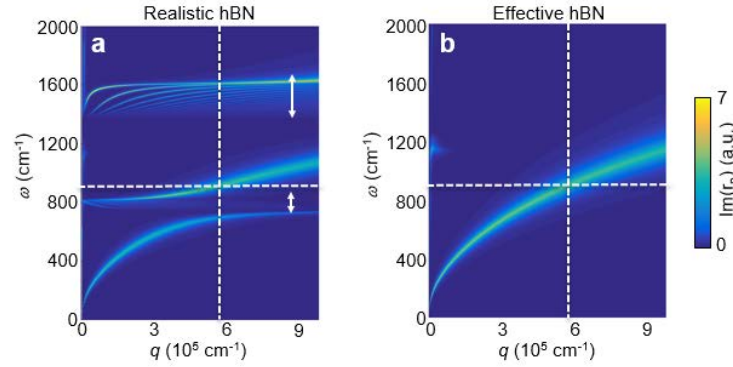


Figure S3. Calculated frequency (ω) – momentum (q) dispersion diagrams of graphene on hBN considering realistic (a) and effective (b) dielectric constants of hBN. Here the realistic dielectric constants of hBN is adopted from previous literature¹⁸ and the effective dielectric constant is set to be 4.0 at $\omega = 910\text{ cm}^{-1}$. The arrows in panel a mark the two reststrahlen bands $746\text{-}819\text{ cm}^{-1}$ and $1370\text{-}1610\text{ cm}^{-1}$ of hBN where graphene plasmons couple strongly with hyperbolic waveguide polaritons in hBN. The horizontal and vertical dashed lines mark the excitation frequency ($\omega = 910\text{ cm}^{-1}$) and corresponding plasmon wavevectors of graphene.

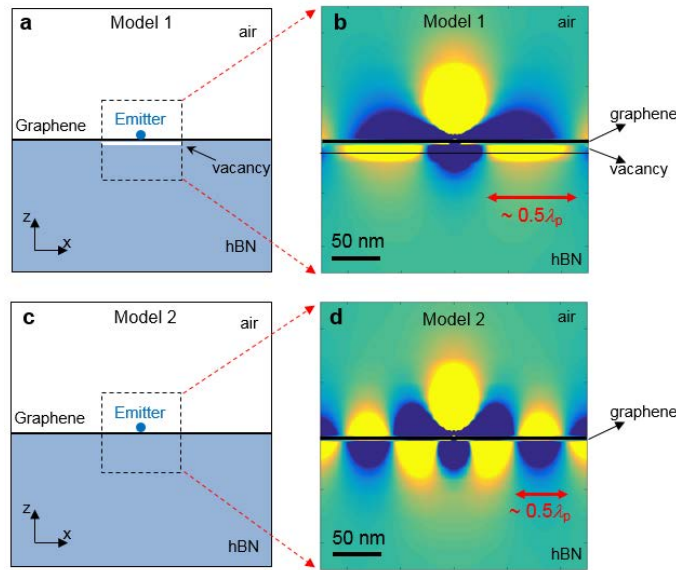


Figure S4. Zoomed-in view of the FDTD simulations (Model 1 and Model 2) shown in Figure 3 of the main text. The zoomed-in regions are marked with dashed squares in panels a and c. The plasmon field maps in these zoomed-in regions are plotted in panels b and d.

The FDTD simulation results of Model 1 and Model 2 are shown in Figure 3 in the main text. In Figure S4, we plot the zoomed-in snapshots of the plasmon field (E_z) maps close to the emitter. As shown in these field maps, the plasmon wavelength (λ_p) in the zoomed-in regions of Model 1 (graphene/air/hBN) is about 70% larger than that in Model 2 (graphene/hBN), consistent with the dispersion calculations in Figure 4 of the main text. As discussed in the main text, the increase of the plasmon wavelength above the bubble/vacancy region is the origin of the plasmon confinement inside the bubbles.

The FDTD simulation results of Model 3 and Model 4 are shown in Figure S5, where we plot the plasmon field (E_z) map of suspended graphene with a Gaussian-shaped graphene bubble at the center (Figure S5c) and that of the completely-flat suspended graphene (Figure S5d), respectively. Similar to Figure 3 in the main text, we plot the zoomed-in views of the region far away from the emitter (marked with rectangles in Figure S5c,d) in Figure S5e,f and the corresponding E_z profiles right above graphene in Figure S5g. In this zoomed-in region, plasmons are the dominant source of field. By comparing Model 3 and Model 4 through these field maps and profiles, one can see that plasmon field of the two models are generally the same indicating that graphene plasmons can propagate freely off the bubble with negligible energy loss despite the curvature. Similar results were also obtained in previous simulation work,¹⁸ where the authors conclude that the high spatial confinement of graphene plasmons is responsible for the negligible radiation loss on slightly-curved graphene. Indeed, the plasmon wavelength ($\lambda_p \sim 100\text{-}200$ nm) is far smaller than the radius of curvature of the bubble (~ 600 nm). The simulation results in Figure S5 prove that pure topographic variations of our nanobubbles are not responsible for the plasmon confinement and hence the hotspots formation inside the bubbles.

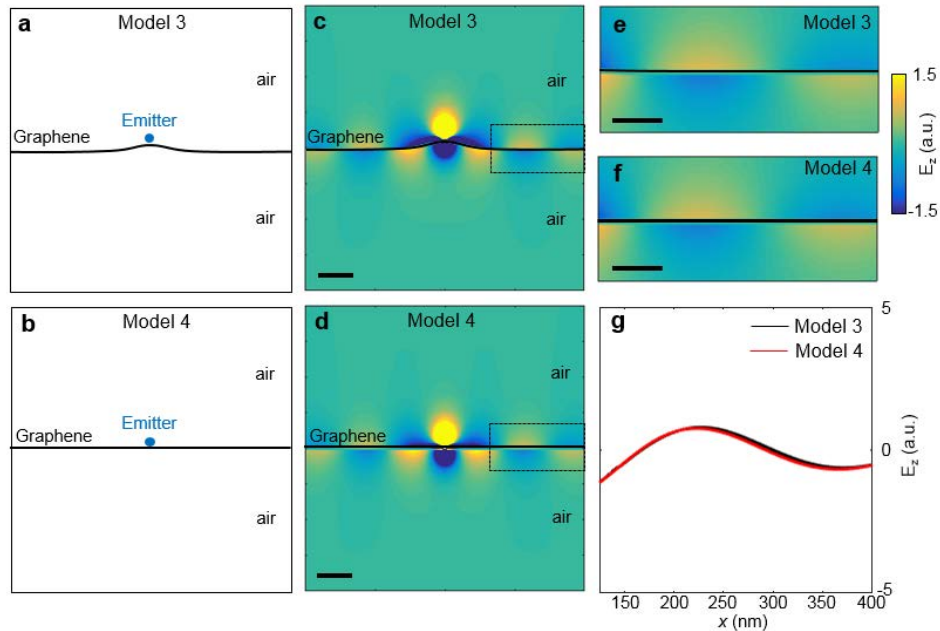


Figure S5. The FDTD simulations of surface plasmon polaritons launched by a point emitter above suspended graphene. (a) Model 3: graphene with a Gaussian-shaped bubble (height = 20 nm; full width at half maximum = 125 nm) at the center right beneath the emitter. (b) Model 4: flat suspended graphene. (c,d) Simulated E_z maps of model 3 and model 4, respectively. (e,f) Zoomed-in E_z maps of the regions defined by rectangles in panels c and d, respectively. (g) Horizontal line

profiles of E_z taken right above the surface of graphene in panels **e** and **f**. Scale bars represent 100 nm in panels **c** and **d**, and represent 50 nm in panels **e** and **f**.

7. Real-space simulation of hotspot patterns in nanobubbles

In order to reproduce the real-space patterns of hotspots distribution, we construct a simplified triangular cavity (Figure S6a). Considering that the nanobubbles that we investigated are relatively flat (height \ll side length), the triangular cavity is a good approximation of the pyramid-shaped bubbles (Figure 1 in the main text). In Figure S6a, we plot the simulated field distribution map $|E_z(x, y)|$ that resembles what we measure in our nano-IR experiments. Here (x, y) are the coordinates of the plasmon source that is scanning over the cavity and $E_z(x, y)$ is the total plasmon field at a given position (x, y) . The purpose of the simulation is for qualitatively understanding the hotspots pattern formation and their dependence with both the plasmon wavelength and bubble size. The tip-launched plasmon field distribution takes the standard circular (cylinder) waveform obtained by solving the Helmholtz equation. We considered mode localization effects by assuming plasmon reflections off the bubble edges. Similar method has been used in an earlier work,¹⁹ where fringes patterns of phonon polaritons of hBN were simulated.

The simulation results are given in Figure S6b-f, where the varying parameter is the ratio between the length of the cavity edge (L) and the graphene plasmon wavelength (λ_p). One can see that, as L/λ_p varies from 2.78 to 0.55 (Figure S6b-f), the $E_z(x, y)$ maps show systematic evolutions. The dominant features of these simulations are the bright hotspots at the corners of the triangular cavity. As L decreases or λ_p increases (e.g. when excitation frequency decreases), the hotspots merge towards the center of the cavity and eventually merge into one single hotspot at the center (Figure S6f). All these features agree well with our imaging data of graphene nanobubbles with different bubble sizes or excitation frequencies (Figure 1 and Figure 2 in the main text).

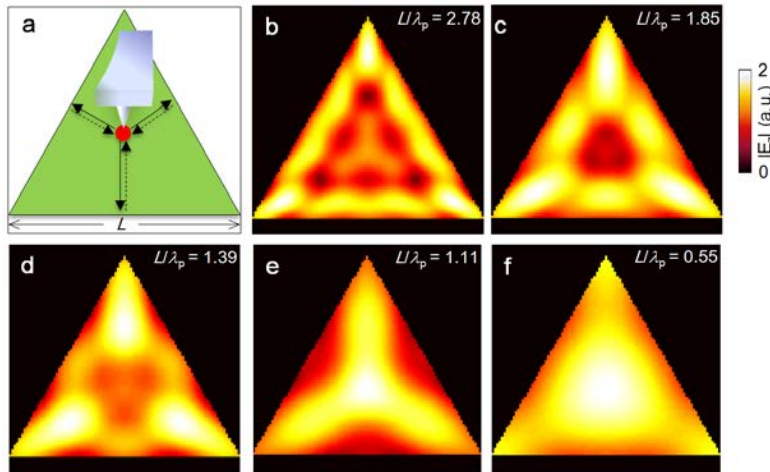


Figure S6. Real-space simulations of plasmonic hotspots inside a triangular cavity. **(a)** Illustration of the triangle cavity for the purpose of real-space simulation. The length of the side is L . **(b-f)** Real-space simulations about $|E_z|$ field amplitude of an equilateral triangle cavity with the ratio L/λ_p from 2.78 to 0.55.

References for the Supporting Information

1. Li, X.; Cai, W.; An, J.; Kim, S.; Nah, J.; Yang, D.; Piner, R.; Velamakanni, A.; Jung, I.; Tutuc, E.; Banerjee, S. K.; Colombo, L.; Ruoff, R. S. Large-area synthesis of high-quality and uniform

graphene films on copper foils. *Science* **2009**, 324, 1312-1314.

2. Dean, C. R.; Young, A. F.; Meric, I.; Lee, C.; Wang, L.; Sorgenfrei, S.; Watanabe, K.; Taniguchi, T.; Kim, P.; Shepard, K. L.; Hone, J. Boron nitride substrates for high-quality graphene electronics. *Nat. Nanotechnol.* **2010**, 5, 722-726.
3. Gannett, W.; Regan, W.; Watanabe, K.; Taniguchi, T.; Crommie, M. F.; Zettl, A. Boron nitride substrates for high mobility chemical vapor deposited graphene. *Appl. Phys. Lett.* **2011**, 98, 242105.
4. Pan, W.; Xiao, J.; Zhu, J.; Yu, C.; Zhang, G.; Ni, Z.; Watanabe, K.; Taniguchi, T.; Shi, Y.; Wang, X. Biaxial compressive strain engineering in graphene/Boron Nitride heterostructures. *Sci. Rep.* **2012**, 2, 893.
5. Choi, S.-M.; Jhi, S.-H.; Son, Y.-W. Effects of strain on electronic properties of graphene. *Phys. Rev. B* **2010**, 81, 081407(R).
6. Pellegrino, F. M. D.; Angilella, G. G. N.; Pucci, R. *Phys. Rev. B* **2010**, 82, 115434.
7. Mayorov, A. S.; Gorbachev, R. V.; Morozov, S. V.; Britnell, L.; Jalil, R.; Ponomarenko, L. A.; Blake, P.; Novoselov, K. S.; Watanabe, K.; Taniguchi, T.; Geim, A. K. Micrometer-Scale Ballistic Transport in Encapsulated Graphene at Room Temperature. *Nano Lett.* **2011**, 11(6), 2396-2399.
8. Baart, T. A. Quantum dots on bilayer graphene made on a substrate of boron nitride using split gates. PhD thesis, Delft University of Technology (2011).
9. Haigh, S. J.; Gholinia, A.; Jalil, R.; Romani, S.; Britnell, L.; Elias, D. C.; Novoselov, K. S.; Ponomarenko, L. A.; Geim, A. K.; Gorbachev, R. Cross-sectional imaging of individual layers and buried interfaces of graphene-based heterostructures and superlattices. *Nat. Mater.* **2012**, 11, 764-767.
10. Manring, L. E. *Macromolecules* **1991**, 24, 3304-3309.
11. Stoliarov, S. I.; Westmoreland, P. R.; Nyden, M. R.; Forney, G. P. *Polymer* **2003**, 44, 883-894.
12. Downing, H. D.; Williams, D. J. *J. Geophys. Res.* **1975**, 80, 1656-1661.
13. Kagarise, R. E. *J. Opt. Soc. Am.* **1960**, 50, 36-39.
14. Soldera, A.; Monterrat, E. *Polymer* **2002**, 43, 6027-6035.
15. Anderson, M. R. Determination of infrared optical constants for single component hydrocarbon fuels. Master Thesis, University of Missouri-Rolla. (2000).
16. Ryu, S.; Liu, L.; Berciaud, S.; Yu, Y.J.; Liu, H.; Kim, P.; Flynn, G. W.; Brus, L. E. *Nano Lett.* **2010**, 10, 4944-4951.
17. Dean, C. R.; Young, A. F.; Meric, I.; Lee, C.; Wang, L.; Sorgenfrei, S.; Watanabe, K.; Taniguchi, T.; Kim, P.; Shepard, K. L.; Hone, J. *Nat. Nanotechnol.* **2010**, 5, 722-726.
18. Banszerus, L.; Janssen, H.; Otto, M.; Epping, A.; Taniguchi, T.; Watanabe, K.; Beschoten, B.; Neumaier, D.; Stampfer, C. arXiv1610.08773v1.
19. Yeh, P. Optical waves in layered media, 2nd edition Wiley-Interscience (2005)
20. Lumerical Solutions, Inc. <http://www.lumerical.com/tcad-products/fdtd>.

21. Lu, W. B.; Zhu, W.; Xu, H. J.; Ni, Z. H.; Dong, Z. G.; Cui, T. J. *Opt. Exp.* **2013**, 21, 10475-10482.
22. Dai, S.; Fei, Z.; Ma, Q.; Rodin, A. S.; Wagner, M.; McLeod, A. S.; Liu, M. K. Gannett, W.; Regan, W.; Watanabe, K.; Taniguchi, T.; Thiemens, M.; Dominguez, G.; Castro Neto, A. H.; Zettl, A.; Keilmann, F.; Jarillo-Herrero, P.; Fogler, M. M.; Basov, D. N. *Science* **2014**, 343, 1125-1129.